PCCP

PAPER

View Article Online
View Journal | View Issue

Cite this: *Phys. Chem. Chem. Phys.*, 2023, **25**, 23614

On the $^{12}C_2H_2$ near-infrared spectrum: absolute transition frequencies and an improved spectroscopic network at the kHz accuracy level†

Antonio Castrillo, [a] Eugenio Fasci, [a] Tibor Furtenbacher, [b] Vittorio D'Agostino, [a] Muhammad A. Khan, [a] Stefania Gravina, [a] Livio Gianfrani *[a] and Attila G. Császár *[b]

Received 21st April 2023,
Accepted 6th July 2023

DOI: 10.1039/d3cp01835k

rsc.li/pccp

Lamb dips of twenty lines in the P, Q, and R branches of the $\nu_1 + \nu_3 + \nu_4^1$ vibrational band of $^{12}C_2H_2$, in the spectral window of 7125–7230 cm^{-1}, have been measured using an upgraded comb-calibrated frequency-stabilized cavity ring-down spectrometer, designed for extensive sub-Doppler measurements. Due to the large number of carefully executed Lamb-dip experiments, and to the extrapolation of absolute frequencies to zero pressure in each case, the combined average uncertainty of the measured line-center positions is 15 kHz (5×10^{-7} cm^{-1}) with a 2-σ confidence level. Selection of the twenty lines was based on the theory of spectroscopic networks (SN), ensuring that a large number of transitions, measured previously by precision-spectroscopy investigations, could be connected to the *para* and *ortho* principal components of the SN of $^{12}C_2H_2$. The assembled SN contains 331 highly precise transitions, 119 and 121 of which are in the *ortho* and *para* principal components, respectively, while the rest remain in floating components. The *para*- and *ortho*-$^{12}C_2H_2$ energy-level lists, determined during the present study, contain 82 and 80 entries, respectively, with an accuracy similar to that of the lines. Based on the newly assembled lists of *para*- and *ortho*-$^{12}C_2H_2$ empirical energy levels, a line list, called TenkHz, has been generated. The TenkHz line list contains 282 entries in the spectral range of 5898.97–7258.87 cm^{-1}; thus far, only 149 of them have been measured directly *via* precision spectroscopy. The TenkHz line list includes 35 intense lines that are missing in the HITRAN2020 database.

1 Introduction

In 2018, Chubb *et al.*[1] published a MARVEL (Measured Active Rotational–Vibrational Energy Levels)[2,3] analysis of the experimentally measured and assigned rovibrational transitions of $^{12}C_2H_2$ available at that time: a total of 37 813 experimental transitions from 61 publications were considered. Ref. 1 complemented earlier reviews, of Herman and co-workers[4–7] and others,[8–10] on the high-resolution spectroscopy of rovibrational states on the ground electronic state of acetylene. From the extended set of measured transitions collated in ref. 1, 5200 *para*- and 6013 *ortho*-$^{12}C_2H_2$ empirical rovibrational energy levels, with usually dependable associated uncertainties, could be determined.

There are several line-by-line spectroscopic databanks, like HITRAN,[11] GEISA,[12] ASD-1000,[10] and ExoMol,[13] usually containing mixed experimental and empirical rovibrational entries on $^{12}C_2H_2$ (and other isotopologues of acetylene). These datasets contain rovibrational energy-level and transition information about acetylene at very different accuracy levels, ranging from a few kHz ($\sim 10^{-7}$ cm^{-1}) to a few hundred MHz (~ 0.01 cm^{-1}). The largest one is the ExoMol line list, ACeTY, which has ~ 4.3 billion rovibrational transitions among ~ 5 million energy levels and it includes wavenumbers up to 10 000 cm^{-1}.[13]

Nowadays, line-center-position measurements can be performed for polyatomic molecular systems at the 10^{-11} relative uncertainty level in the near-infrared portion of the electromagnetic spectrum. These precision-spectroscopy measurements are made possible by a combination of optical frequency-comb synthesizers with the most advanced cavity-enhanced spectroscopic methods. In particular, exploiting the resonant enhancement of the intracavity optical power, Lamb-dip observations are possible for weak overtone transitions. These measurements facilitate the determination of highly accurate line-center positions.[14,15] Non-linear mixing techniques allow these

[a] *Department of Mathematics and Physics, Università degli Studi della Campania "Luigi Vanvitelli", 81100, Caserta, Italy. E-mail: livio.gianfrani@unicampania.it*
[b] *Laboratory of Molecular Structure and Dynamics, Institute of Chemistry, ELTE Eötvös Loránd University and MTA-ELTE Complex Chemical Systems Research Group, Pázmány Péter sétány 1/A, H-1117 Budapest, Hungary. E-mail: attila.csaszar@ttk.elte.hu*

† Electronic supplementary information (ESI) available. See DOI: https://doi.org/10.1039/d3cp01835k

determinations to be extended to longer wavelengths, throughout the mid-infrared region.[16,17]

A considerable number of transitions have been measured for acetylene isotopologues with close to kHz accuracy.[18–33] In this regard, the comprehensive study of ref. 1 concerning the experimental spectroscopic measurements on the parent isotopologue, $^{12}C_2H_2$, should be considered incomplete: at the time the MARVEL dataset was assembled, results from several important precision-spectroscopy studies were simply not available and a few existing ones were not utilized to their full extent. As of today, the precision-spectroscopy measurements available on $^{12}C_2H_2$ include the $\nu_1 + \nu_3$,[21,22,29] $2\nu_3 + \nu_5$,[1,32] and $\nu_1 + 3\nu_3$[30] bands, as well as ν_4- and ν_5-excited hot bands,[27] involving wavenumber regions around 6500, 7200, and 12 700 cm^{-1}. Highly-accurate measured transitions are also available for the ν_5–ν_4 difference band[25] (see Table 1 for the meaning of the quantum numbers used to designate the vibrational bands as well as for the vibrational fundamentals of $^{12}C_2H_2$[1,34,35]). For $^{12}C_2H_2$, many of the precision-spectroscopy measurements provided lines which do not connect with each other, hindering the full utilization of these accurate transitions in an improved understanding of acetylene spectroscopy. It should also be mentioned that the accuracy of these precision-spectroscopy measurements[21,22,25,27,30,32] have not been checked against each other in a consistent manner (see the related critique of ref. 1 above).

There are several reasons why the knowledge of transition frequencies with very high accuracy is important for acetylene.[1,4–6,8,36,37] First, there are several rovibrational transitions in coincidence with the International Telecommunication Union's C-band, situated at 1530–1560 nm, that are ideally suited to satisfy the demand of improved frequency standards to be used in telecommunication for the aims of wavelength division multiplexing. Second, the near-infrared spectrum of acetylene is of considerable interest in the field of optical frequency metrology: (a) the P(16) $\nu_1 + \nu_3$ transition of $^{13}C_2H_2$ has been included by the International Committee for Weights and Measures (CIPM) in the list of recommended reference lines for the practical realization of the definition of the meter, and (b) acetylene was used as a molecular target in Doppler-broadening gas thermometry for the optical determination of the Boltzmann constant,[36] and subsequently enabled for the implementation of the new SI definition of the unit Kelvin.[37] Third, the acetylene spectrum can be extremely useful for studying the atmosphere of young Earth-like exoplanets,[38,39] requiring the availability of high-quality spectroscopic parameters.

To increase the number of acetylene lines known at the kHz accuracy level and make the best use of the previously determined ones, we decided to undertake a measurement campaign using the modern technique of comb-calibrated frequency-stabilized cavity ring-down spectroscopy (CC-FS-CRDS).[40–42] Our experimental study was designed with several goals and achievements in mind. Our first aim was to simplify and upgrade the cavity ring-dwon (CRD) spectrometer in Caserta to facilitate extensive precision-spectroscopy measurements while preserving the same level of accuracy as reported in ref. 32. Part of the apparatus improvement involved building a CRD spectrometer in a more compact way using fiber-coupled and integrated optics devices, thus reducing as much as possible the optical path length in air (see Fig. 1). This helps to avoid laser attenuation due to water absorption in air, which likely occurs during our measurements. Second, after checking the connectivity and the accuracy of existing ultraprecise measurements *via* tools offered by the theory of spectroscopic networks,[43–46] our aim was to assemble the largest possible list of rovibrational energies and transitions, all known at the kHz accuracy level. The SN approach allows the transfer of the high experimental accuracy, in the kHz regime in the present case, to the empirical energy values derived and the line positions predicted. These energy and transition lists should supplement databanks containing entries which are orders of magnitude less accurate. As part of this effort, our aim was to connect at present unconnected components and orphans to the *para* and *ortho* principal components of the SN of $^{12}C_2H_2$ *via* a small set of carefully selected newly measured transitions. For example, in ref. 27 there are 135 measured transitions within two hot bands and none could be connected with other kHz-accuracy measurements prior to the present work.

Table 1 Conventional quantum numbers, corresponding to the normal-mode (harmonic-oscillator) picture for the vibrations and the rigid-rotor picture for the rotations, used to label the rovibrational states of $^{12}C_2H_2$ and wavenumbers, in cm^{-1}, of the fundamentals

Label	Description (symmetry)	Fundamental
v_1	CH symmetric stretch (σ_g^+)	3372.8491(1)[35]
v_2	CC symmetric stretch (σ_g^+)	1974.317(6)[1]
v_3	CH antisymmetric stretch (σ_u^+)	3294.840(2)[1]
v_4	Symmetric (*trans*) bend (π_g)	612.871(2)[34]
l_4	Vibrational angular momentum associated with v_4	
v_5	Antisymmetric (*cis*) bend (π_u)	730.332(2)[34]
l_5	Vibrational angular momentum associated with v_5	
L	Total vibrational angular momentum, $\lvert l_4 + l_5 \rvert$	
J	Rotational angular momentum quantum number	
e/f	Rotationless parity of the rovibrational state	

2 Experimental details

2.1 Apparatus

In this study, saturated absorption spectra were acquired using a comb-calibrated frequency-stabilized CRD spectrometer. Schematically shown in Fig. 1, the set-up is an upgraded and simplified version of the apparatus described in ref. 32. The main element of novelty is the use of just one laser referenced to an optical frequency-comb synthesizer. In addition, extensive use was made of fiber optic components and devices to make the spectrometer more compact. The set-up essentially consists of three modules: (i) a 10 kHz-linewidth laser source, referred to as the probe laser (PL); (ii) an absolute frequency calibration unit; and (iii) a high-finesse ring-down optical resonator (HFOR).

The probe laser is an external-cavity diode laser (ECDL) with an emission wavelength in the range between 1.38 and 1.41 μm.

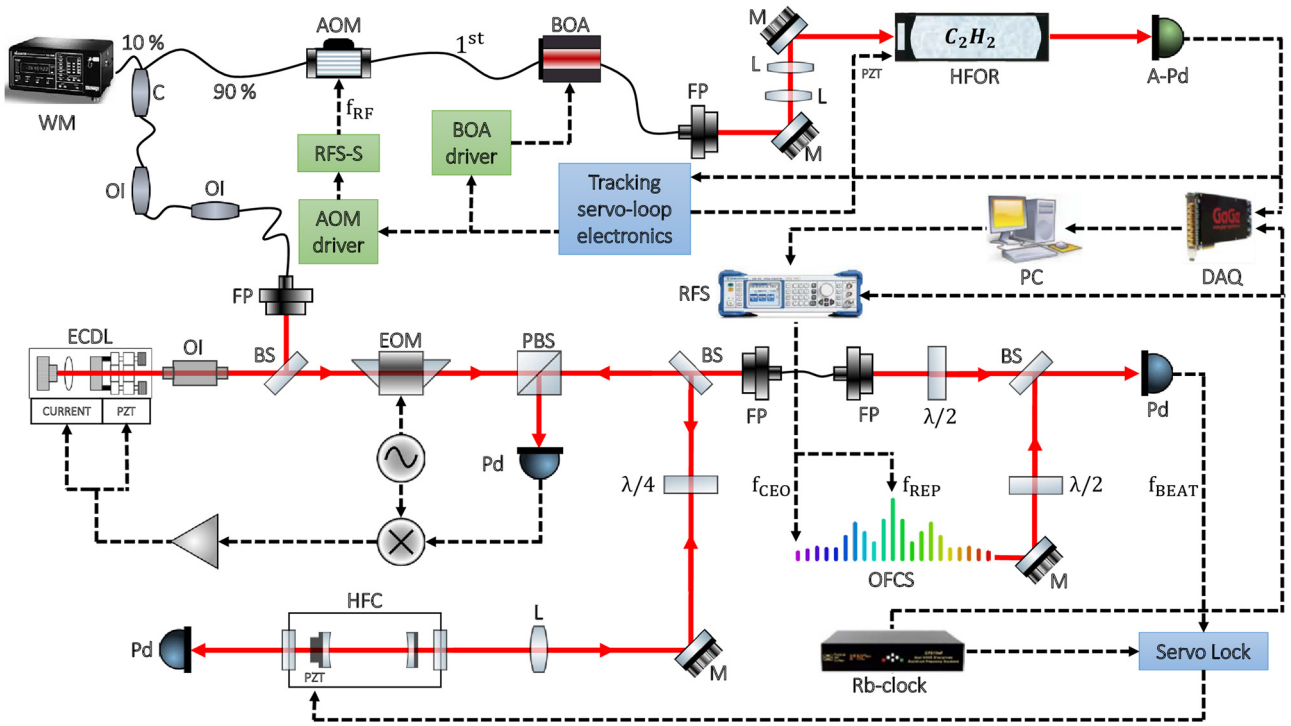

Fig. 1 Cartoon depicting the comb-calibrated frequency-stabilized cavity ring-down spectroscopy (CC-FS-CRDS) apparatus utilized during this study. ECDL: external-cavity diode laser; M: mirror; L: lens; BS: beam splitter; PBS: polarizing beam splitter; λ/4: quarter-wave plate; λ/2: half-wave plate; HFC: high-finesse cavity; OFCS: Rb-clock disciplined optical frequency comb synthesizer; Pd: photodiode; RFS: radio-frequency synthesizer; FP: fiber-port; OI: optical isolator; C: fiber coupler; WM: wavemeter; EOM: electro-optic modulator; AOM: 40 MHz fiber-coupled acoustic-optic modulator; RFS-S: radiofrequency switches; BOA: booster optical amplifier; PZT: piezoelectric transducer; APd: avalanche photodiode; HFOR: high-finesse optical resonator; PC: personal computer; DAQ: data acquisition board. Continuous black lines represent fiber connections; dotted black lines electrical connections, and continuous red lines the free-air laser path.

As already described in ref. 47, in order to reduce its emission linewidth the ECDL was tightly locked to a high-finesse optical cavity (HFC) by means of the Pound–Drever–Hall technique. The absolute frequency calibration unit is based upon a self-referenced optical frequency-comb synthesizer (OFCS, from Menlo Systems, model FC1500-250-WG), stabilized against the 10 MHz time-base signal from a GPS-disciplined Rb clock. The HFC is weakly locked to one of the comb teeth, with an offset frequency, f_{BEAT}, of 20 MHz. This technical expedient has twofold advantage: on the one hand, it allowed us to determine the absolute frequency of the probe laser, on the other hand, we could straightforwardly perform calibrated frequency scan of PL around a selected $^{12}C_2H_2$ transition. In fact, the PL frequency, f_{PL}, which is given by the equation $f_{PL} = N \times f_{REP} \pm f_{CEO} \pm f_{BEAT} + f_{RF}$, could be finely tuned by a variation of the comb repetition rate (through an external electrical frequency synthesizer referenced to the GPS-disciplined Rb oscillator). In the f_{PL} equation, N represents the comb tooth order, while f_{REP} = 250 MHz, f_{CEO} = 20 MHz, and f_{RF} are the comb repetition rate, the carrier envelope offset frequency, and the RF frequency driving the acousto-optic modulator (AOM), respectively. For each of the investigated transitions, the ± signs were easily determined by slightly varying f_{CEO} and f_{REP} and observing the subsequent variation of f_{BEAT}, whereas the tooth order was obtained by measuring the PL wavelength by means of a 7-digit wavemeter. The relative stability of the entire frequency chain is 2.5×10^{-12}, limited by the frequency stability of the Rb clock.[37]

The HFOR consists of two plano-concave high-reflectivity mirrors, spaced 43 cm apart by a Zerodur block. The mirrors have a radius of curvature of 1 m and a nominal reflectivity greater than 99.99%. One of the mirrors is equipped with a piezo transducer for a fine tuning of the cavity length. The finesse of the cavity was about 230 000 (corresponding to a ring-down time under vacuum conditions of about 105 μs), while the cavity-mode width was 1.5 kHz. At the output of the cavity, an InGaAs avalanche detector (APd, with an effective bandwidth of 420 kHz and a noise-equivalent power of 0.46 pW $Hz^{-1/2}$) monitored the light emerging from the resonator. A digital acquisition board (DAQ) was used to record the ring-down events. The DAQ works at a sample rate of 10^7 samples s^{-1}, its vertical resolution being 16 bit.

A portion of the PL beam was sent into a pair of fiber-coupled optical isolators, followed by a fiber-coupled AOM, whereas the first-order diffracted beam was coupled to the HFOR by means of a mode-matching telescope. The frequency of the laser light emerging from the AOM was up-shifted by a constant amount f_{RF} = 40 MHz (as monitored by a universal counter not shown in Fig. 1). The AOM was also used as an optical switch to initiate ring-down decays. This was accomplished by means of a pair of radio-frequency switches, ensuring an extinction ratio of about 90 dB. Before entering the resonator, the first-order beam

was amplified by a fiber-coupled booster optical amplifier (BOA) up to about 20 mW. The signal produced by the APd on the cavity transmission was used as input to a threshold detector in order to monitor whether a resonance condition takes place while scanning the PL frequency. The threshold detector unit was part of the tracking servo-loop circuit that allows for high-resolution spectral acquisitions.[48] Moreover, the threshold detector was set so that only the occurrence of a TEM_{00} excitation could be detected. In this case, a TTL trigger signal was produced and sent to the AOM switches and to the BOA driver in order to suddenly switch off the laser beam. The same TTL pulse simultaneously triggered the DAQ, while its internal clock was locked to the GPS Rb standard. The duration of the TTL signal was 700 μs, namely, about a factor of 7 larger than the ring-down time under vacuum conditions.

The CRD spectrometer is characterized by doing repeated acquisitions of empty cavity ring-down events. The Allan deviation analysis of such datasets led to an estimation of the minimum detectable absorption coefficient, given by 7.8×10^{-12} cm^{-1}, while the noise equivalent absorption (NEA) figure was 8.4×10^{-11} cm^{-1} $Hz^{-1/2}$.

Under our experimental conditions, the comb tooth order (N) is around 860 000 and a 12.5 Hz wide scan of f_{REP} corresponds to an optical frequency tuning of about 10 MHz. This is sufficiently wide to allow recording the Lamb-dip feature for all the selected rovibrational lines. This is another element of novelty as compared to ref. 32, in which laser scans were more than a factor of 200 larger. In particular, PL scans were performed setting a frequency step of f_{REP} = 0.025 Hz, thus resulting in a Lamb-dip spectrum consisting of 500 spectral points. For each of them, twenty repeated acquisitions of the exponential decay were performed. As a consequence, at the end of each PL scan across the selected transition, 10 000 ring-down events were collected. A LabView code, expressly developed to implement this experimental strategy, was used to control the frequency of the repetition rate, to guide the data acquisition board, and to collect ring-down events.

2.2 Data analysis and line-center-frequency determinations

The dataset associated with each ring-down event was analyzed by means of a fit to an exponential decay function. The decay time, $\tau(\tilde{\nu})$, was then converted into total loss per unit length (in cm^{-1}) according to the well-known relation

$$\frac{1}{c\tau(\tilde{\nu})} = \alpha(\tilde{\nu}) + \frac{1}{c\tau_0}, \quad (1)$$

where $\tilde{\nu}$ is the PL wavenumber (in cm^{-1}), c is the speed of light (in cm s^{-1}), $\alpha(\tilde{\nu})$ (in cm^{-1}) is the absorption coefficient of the gas sample, and τ_0 is the ring-down time (in s) under vacuum conditions. An example of a recorded Lamb-dip is shown in panel (a) of Fig. 2.

It is important to note that the ring-down decay curve should deviate from the exponential behavior when the absorption is saturated.[49] Nevertheless, since the intracavity power was much smaller than the saturation power of the investigated transitions, we could effectively model the decay curve with a pure exponential function.

In the fitting procedure, the Lamb-dip feature, $\alpha(\tilde{\nu})$, was modeled by the following equation:

$$\alpha(\tilde{\nu}) = g_B(\tilde{\nu}) - A_L \times g_L(\tilde{\nu} - \tilde{\nu}_{L0}), \quad (2)$$

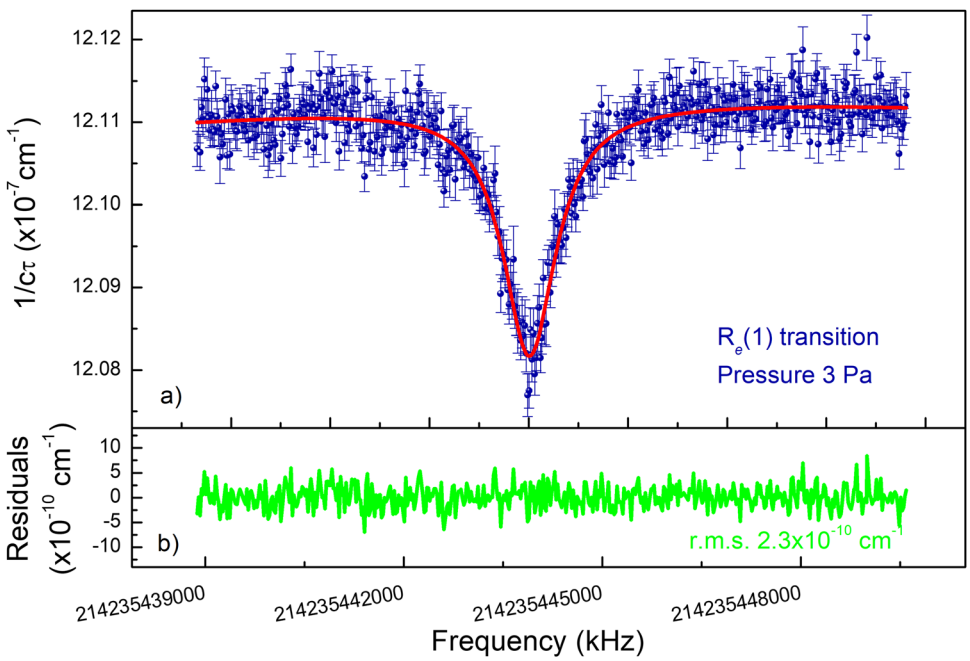

Fig. 2 Panel (a): Example of a Lamb-dip spectrum for the R_e (1) line at a pressure of 3.0 Pa. The spectrum consists of 500 data points with a frequency step of 20 kHz. Panel (b): example of residuals, as obtained from the application of the fitting procedure.

where $g_B(\tilde{\nu})$ is a quadratic baseline, A_L is the amplitude of the Lamb-dip, and $g_L(\tilde{\nu} - \tilde{\nu}_{L0})$ is given by an area-normalized Lorentzian lineshape function having its line center frequency at $\tilde{\nu}_{L0}$. Panel (b) of Fig. 2 shows the fit residuals, computed as the difference between the experimental spectrum and that calculated with eqn (2). In the fitting procedure, the Lorentzian width, Γ_L, as well as A_L, $\tilde{\nu}_{L0}$, and the three coefficients of the quadratic term were considered as free parameters. The typical deviation between theory and experiment turned out to be comparable to the noise level. In the case of Fig. 2, the root mean square (rms) of the residuals was 2.3×10^{-10} cm^{-1}. This translates into a signal-to-noise ratio (SNR) of about 20. Similar values were found for all the investigated transitions. The residuals provide no signatures of line asymmetry. It is worth noting that the width of the sub-Doppler features was always smaller than 1 MHz. The various contributions to the width will be discussed later in this Section.

For a given gas pressure, four consecutive spectra were acquired and analyzed, so as to have four repeated values of $\tilde{\nu}_{L0}$. Subsequently, the line center frequency was retrieved as the mean value of the dataset. The procedure was repeated for other five pressures, in the range of 0.5–3 Pa. A weighted linear fit of these determinations as a function of the C_2H_2 pressure allowed us to extrapolate the zero-pressure value of the line center frequency, as it is shown in Fig. 3 for the $R_e(4)$ transition. For each of the investigated transitions, this procedure was carried out at least three times, over a period of one week, so as to have repeated determinations of the Lamb-dip zero-pressure center frequency. Once this experimental strategy was completed, the final value of the line-center frequency could be determined as the weighted mean, $\bar{f}_{wm}$, of the whole dataset. As far as the statistical uncertainty is concerned, it was calculated after a consistency test, as provided by the *Bureau International des Poids et Mesures* (BIPM) and reported in Appendix 1 of ref. 50. In particular, we compared the experimental chi-square, χ^2_{exp}, with the degrees of freedom, m, as well as with the 95 percentile of the theoretical chi-square, χ^2_{theor}, corresponding to m. In the case of a successful consistency test, namely when $\chi^2_{exp} < \chi^2_{theor}$ and $\chi^2_{exp} < m$, the uncertainty, $u_{\bar{f}_{wm}}$, was calculated as the usual uncertainty of a weighted mean. In the other cases, a correction to $u_{\bar{f}_{wm}}$ was applied according to the equation $u_{\bar{f}_{wm,corr}} = u_{\bar{f}_{wm}} \sqrt{\chi^2_{exp}/m}$.

The entire experimental procedure was applied to a carefully chosen set of *para* and *ortho* lines of the P, Q, and R branches of the $\nu_1 + \nu_3 + \nu_4{}^1$ vibrational band of $^{12}C_2H_2$. Line assignments, absolute center frequencies and associated uncertainties at the 2-σ confidence level are reported in Table 2.

The uncertainty quoted for each transition includes both statistical and systematic contributions. In particular, the statistical uncertainty ranges between 7 to 18 kHz. The systematic contributions were quoted according to the outcomes of ref. 32. The main source of uncertainty could be ascribed to the measurement of the pressure, provided by the absolute pressure gauge that was used (MKS, model 122A), having a full scale and a sensitivity of 1000 Pa and 0.1 Pa, respectively. Since the pressure values enter into each zero-pressure frequency determination, their uncertainty influenced the accuracy of our determinations. To this end, for one of the datasets, we have repeated the weighted linear fit adopting two different pressure scales, in which the pressure readings were decreased and increased by 0.1 Pa, this latter value being the last digit given

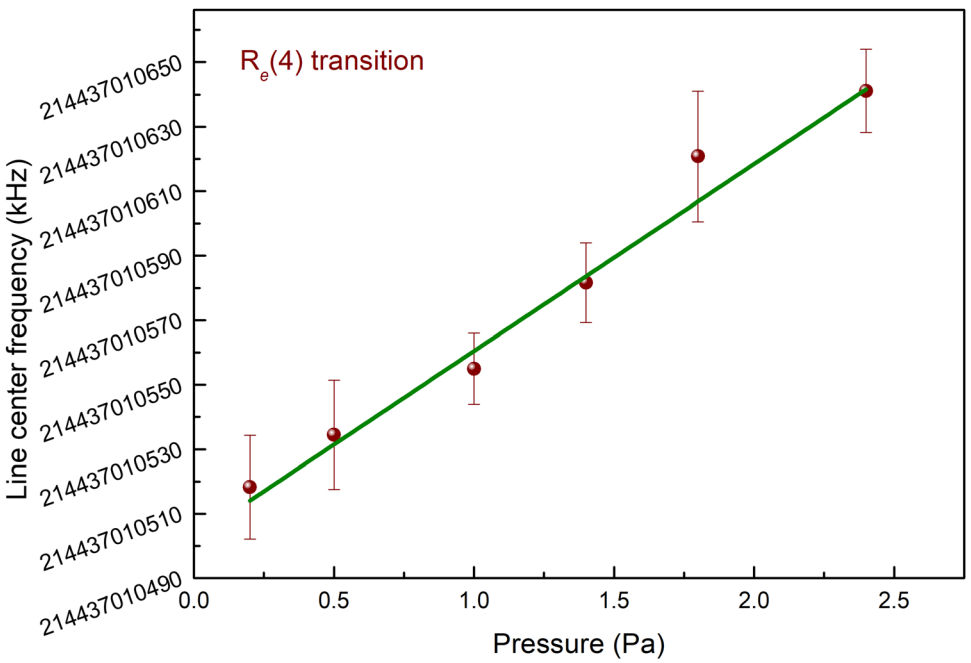

Fig. 3 An example showing a set of measurements for the $R_e(4)$ transition, from which the zero-pressure absolute frequency can be retrieved. For this dataset, the slope is 58(4) kHz Pa^{-1}.

Table 2 Twenty newly-measured ultraprecise rovibrational transitions for the $\nu_1 + \nu_3 + \nu_4^1 \equiv (1\,0\,1\,1^1\,0^0)^1$ band on the ground electronic state of the $^{12}C_2H_2$ molecule, sorted by their frequencies. The individual uncertainties correspond to 2-σ confidence level and include both statistical and systematic contributions

Band	Line	Frequency (kHz)	Expt. uncertainty (kHz)
$(1\,0\,1\,1^1\,0^0)^1$	P_e (6)	213 661 027 647	14
	P_e (5)	213 735 751 551	17
	P_e (3)	213 882 700 887	14
	Q_{ef} (16)	214 027 218 629	13
	Q_{ef} (14)	214 043 109 327	20
	Q_{ef} (13)	214 050 282 791	14
	Q_{ef} (12)	214 056 942 021	19
	Q_{ef} (11)	214 063 087 282	14
	R_e (0)	214 166 572 014	12
	R_e (1)	214 235 443 830	15
	R_e (2)	214 303 474 931	12
	R_e (3)	214 370 664 215	15
	R_e (4)	214 437 010 514	16
	R_e (10)	214 817 321 921	14
	R_e (11)	214 877 735 999	16
	R_e (12)	214 937 298 310	12
	R_e (13)	214 996 008 080	21
	R_e (14)	215 053 864 720	18
	R_e (15)	215 110 867 741	14
	R_e (16)	215 167 019 970	20

by the pressure gauge. Doing so, we could include a systematic contribution of 9 kHz in the uncertainty budget. The OFCS contributes with an uncertainty of 1 kHz, which is due to the stability of the GPS-disciplined Rb clock. Moreover, while the recoil shift cancels out in Lamb-dip spectroscopy,[51] the second-order Doppler shift has been estimated taking into account the root-mean square velocity of the C_2H_2 molecules. Under our experimental conditions, it amounts to 0.7 kHz. We did not observe any influence in the retrieved line-center frequencies from the power coupled into the HFOR cavity. However, adopting a very cautious approach, we decided to add a further contribution of 0.8 kHz due to the power shift, according to the outcomes of ref. 52. A further component we considered takes into account the frequency difference between the PL and the cavity resonance.[40] Its estimation amounts to 0.4 kHz. The uncertainties associated to the driving frequency of the AOM, to the wave-front curvature, as well as to that coming from possible interfering lines were estimated to be negligible. To summarize, the transition frequencies reported in this work were determined with an overall uncertainty ranging between 12 and 21 kHz in a 2-σ confidence interval.

It is worth noting that the pressure-shifting coefficient, δ, of the twenty lines investigated in this work varies from 3 to ~70 kHz Pa^{-1}. A few lines exhibit relatively large values of δ compared to those measured for other C_2H_2 lines in other spectral regions, also in the sub-Doppler regime.[30,31] There are examples of anomalies in pressure-shifting coefficients from sub-Doppler experiments. For instance, in 2018, Chen *et al.*[53] measured a self-shifting of +14 kHz Pa^{-1} for a water line at 790 nm, a value that is quite different from −5 kHz Pa^{-1} given in HITRAN. Similarly, Cozijn *et al.*[54] measured a pressure-dependent shift of −9 kHz Pa^{-1} for a sub-Doppler rovibrational line of HD, providing evidence that this collisional-shift coefficient was an order of magnitude larger than the typical coefficients for H_2, obtained from Doppler-limited studies. Investigating the reason for these anomalies is out of the scope of the present paper and may be eventually the subject of a future article. Nevertheless, we believe that this issue does not influence the extrapolated zero-pressure value of the line center frequency.

2.3 Measurement conditions

Several $^{12}C_2H_2$ vibrational bands fall within the spectral region covered by the ECDL. For the aims of the present study, 20 lines belonging to the $\nu_1 + \nu_3 + \nu_4^1$ band were selected, showing an Einstein coefficient, A, in the interval 0.015–0.050 s^{-1}.[11] Combined with the population distribution at room temperature, these A values lead to line intensities which do not exceed 9×10^{-23} cm $molecule^{-1}$.[11] These particular characteristics allowed the detection of Lamb-dip signals under a weak saturation regime. In fact, for the transition showing the highest A value, taking into account that the experimental full width at half-maximum (FWHM) of the observed Lamb-dip never exceeds the 1 MHz value, we calculated a saturation intensity, I_{sat}, of about 1×10^8 W m^{-2}.[55] According to the formula given in ref. 56 and considering a 0.05% mode-matching parameter, we estimate that the intracavity intensity, I_{cav}, was much smaller than I_{sat}, the saturation parameter G being ~0.007.

As shown in Fig. 2, the FWHM of the recorded Lamb dip is 850 kHz, as retrieved from the Lorentzian fit. Such a width is in partial agreement with the joint effect of various broadening mechanisms, namely, the transit time broadening (of about 255 kHz for a cavity waist of 430 μm and a gas temperature of 296 K), the intracavity power broadening, which increases the linewidth by a factor of $\sqrt{1+G}$, and the 310 kHz collisional broadening that can be calculated using the self-broadening coefficient reported in HITRAN.[11] This discrepancy can be ascribed to the fact that the self-broadening coefficient from Lamb-dip experiments can be up to one order of magnitude larger than that retrieved in the Doppler regime.[31]

3 Theoretical details

3.1 Labels

Table 1 explains elements of the label used to denote rovibrational states of $^{12}C_2H_2$. The vibrational states are labelled as $\left(v_1 v_2 v_3 v_4^{l_4} v_5^{l_5}\right)$. Note that $|l| = v, v-2, \ldots, 1$ for odd v and $|l| = v, v-2, \ldots, 0$ for even v. The rotational part of the label includes the traditional J and K quantum numbers, where J is an exact quantum number describing the overall rotation of the molecule and the approximate quantum number K corresponds to the projection of the rotational angular momentum onto the principal axis of acetylene. Overall, $\left(v_1 v_2 v_3 v_4^{l_4} v_5^{l_5}\right)^K$, J, and e/f is used to denote the rovibrational states. e/f is used to denote the rotationless parity of the rovibrational states. For further details about elements of the label and the selection rules the reader may want to consult ref. 1.

3.2 Marvel

MARVEL, standing for Measured Active Rotational–Vibrational Energy Levels,[2,3] is an inversion technique yielding empirical energies with dependable uncertainties from measured transitions, all equipped with uncertainties and unique labels. MARVEL is based on the theory of spectroscopic networks (SN).[43–45] This is basically the same procedure, except for the handling of uncertainties, as used in ref. 1.

Since H is a fermion with a nuclear spin of 1/2, $^{12}C_2H_2$ has two nuclear-spin isomers, traditionally called *para* and *ortho*. The energy difference between the lowest *para* and *ortho* states is colloquially called the 'magic number'.

One way to derive the absolute energy of the lowest *ortho* state involves a fit of an effective Hamiltonian model (usually not a global but a local one, considering only the ground vibrational state) to a large number of energy differences. In ref. 7, results of a global fit are reported and the magic number can be taken as 2.3 532 864 cm^{-1}. Considering the experimental accuracy of the lines utilized during the global fit, the accuracy of this magic number is roughly 3 MHz (9×10^{-5} cm^{-1}), which is orders of magnitude larger than the accuracy of the measurements dealt with here.

Clearly, none of the empirical *ortho* energy values can have an absolute uncertainty better than that of the magic number upon which they are based, not even those involved in accurate precision-spectroscopy measurements. Therefore, in this study two separate energy-level lists are provided, one for the *para* and one for the *ortho* principal components, whereby the energies of the lowest states are both set to zero with zero uncertainty. While this way we cannot provide absolute energies for the *ortho*-$^{12}C_2H_2$ principal component, this issue does not affect the accuracy of the transitions of the linelist to be assembled. It is left to future well-designed precision-spectroscopy measurements to determine the magic number of $^{12}C_2H_2$ with kHz accuracy, similar to how it was done for $H_2{}^{16}O$[57] and $H_2{}^{18}O$.[58]

3.3 Ultraprecise spectroscopic network of $^{12}C_2H_2$

Accuracy has central importance for the present study. Thus, each source was carefully checked about the proper meaning and magnitude of the reported uncertainties of the measured lines. It should also be noted here that there are two important elements of graph/network theory[59] which help to ascertain and secure the accuracy of the empirical energy levels and the experimental transitions of SNs: paths and cycles. Paths in a SN secure the formation of energy differences for any pair of the participating states. The redundancy inherent to cycles of the SN provides a powerful self-checking feature; most importantly, cycles can be used to confirm the accuracy of the associated transitions.

The measurement uncertainty, 1-σ of the combined type (statistical plus systematic), of the source 96NaLaAwKo[19] is larger than 100 kHz. The same can be said about the source 09YuDrPe[25]. While these are excellent measurements on their own right, we decided not to consider these sources during the present study. Neglecting the transitions reported in 96NaLaAwKo[19] has no real effect on our analysis since 06MaAlCzBe[22] reported the same lines with significantly lower uncertainties.

The sources we considered during our combined experimental and theoretical study of precision-spectroscopy measurements on $^{12}C_2H_2$ are listed in Table 3. The number of ultraprecise lines available in each source is listed under *A* (available). The number of lines validated (*V*) either with (V_{after}) or without (V_{before}) the newly measured transitions of this study are indicated in the third column of Table 3. The measurement range and the average and maximum uncertainties of the lines are also given there.

The source 18TaHuSuWa[30] contains two unassigned lines; thus, only 43 transitions out of the 45 given in Table 2 of ref. 30 could be utilized in this study. We could not find reasonable assignments for the two unassigned lines.

A constant pressure of 2.7 ± 0.6 Pa (20 ± 5 mTorr) was maintained inside the chamber throughout the measurements reported in 06MaAlCzBe[22] and the pressure shift of each line was not measured. The pressure shift assumed, +1 kHz Pa^{-1}, is likely to be too small and it may even have an incorrect sign, in some cases. Furthermore, the effect of impurities cannot be cancelled out completely at finite pressures. This is the reason why we did measurements as a function of the gas pressure, so we can get rid of any issue related to impurities, which influence the pressure shifting coefficient, and retrieved the zero-pressure value of the line-center frequency. While the reported uncertainties of ref. 22

Table 3 Sources contained in the precision-spectroscopy database of $^{12}C_2H_2$, with ranges and uncertainties (unc., Avg. = average and Max. = maximum). The uncertainties listed correspond to 2-σ confidence level. *A* is the number of lines available in the given source, while V_{before} and V_{after} provide the number of lines validated (*V*) either with (V_{after}) or without (V_{before}) the newly measured transitions of this study

Source tag	Range/cm^{-1}	$A/V_{before}/V_{after}$	Avg. unc./cm^{-1}	Max. unc./cm^{-1}
05EdBaMaGi[21]	6471.75 634–6578.57 589	41/41/41	7.1×10^{-7}	1.4×10^{-6}
06MaAlCzBe[22]	6471.75 634–6617.99 087	63/63/63	1.6×10^{-7}	6.1×10^{-7}
09KnWuLiTi[24]	6523.87 924–6523.87 924	1/1/1	6.2×10^{-7}	6.2×10^{-7}
13WaWhFoGr[26]	6523.87 924–6523.87 924	1/1/1	6.2×10^{-7}	6.2×10^{-7}
15TwCiSeMc[27]	6448.34 318–6564.17 703	135/0/48	3.6×10^{-7}	1.5×10^{-6}
16GaGoGaBe[29]	6474.86 134–6487.03 740	3/3/3	1.2×10^{-7}	1.3×10^{-7}
18TaHuSuWa[30]	12 612.32 392–12 713.38 603	43/43/43	2.2×10^{-7}	2.4×10^{-7}
18TwHaSe[31]	6452.61 818–6471.75 634	7/3/3	2.7×10^{-7}	4.0×10^{-7}
21FaGrPoCa[32]	7167.18 980–7216.97 672	16/16/16	5.3×10^{-7}	8.7×10^{-7}
22AiSaDeRo[33]	6561.09 411–6561.09 411	1/1/1	8.0×10^{-8}	8.0×10^{-8}
This work: 23CaFaAgKh	7126.96 474–7177.19 923	20/0/20	5.3×10^{-7}	8.1×10^{-7}

may be slightly optimistic, our analysis of the cycles these transitions participate in did not suggest that we needed to increase the original uncertainties to the carefully updated BIPM-corrected[60] values.

In the source 15TwCiSeMc[27] the uncertainty reported is 1-σ of the combined type. Four of the measured transitions form a cycle whereby the discrepancy is too large. Multiplication of the line uncertainties by 1.5 solves the discrepancy problem. Therefore, we decided to multiply all the uncertainties of this source by a factor of 1.5. Note that this is the only source where our checking indicated that the source uncertainties need to be increased.

Without the transitions of the present study, none of the large number of lines of 15TwCiSeMc[27] connect to the two principal components of $^{12}C_2H_2$, disallowing their validation and their true utilization when it comes to predicting new transitions accurately. Based on the new measurements of this study, some of the floating components originating in this source are now part of the SN.

The source 18TwHaSe[31] reports, with 1-σ uncertainties of the statistical type, seven nearly-kHz-accuracy lines near to 1.5 μm ($\nu_1 + \nu_3$ band). Only three of the seven measured lines connect to the principal components, since the J values of the lower states are high (>31). Within the experimental constraints of the present study no further transitions could be connected to the principal components.

The true accuracy of the measurements can be tested *via* the even-membered cycles[46] they form (see Fig. 4). The original precision-spectroscopy measurements form 66 four-membered cycles. It is comforting to know that the transitions of the sources given in Table 3 achieve self-consistency with the original 2-σ uncertainties, that is an increase of uncertainties, based on these cycles, turned out not to be necessary.

Careful selection of the lines to be measured followed guidelines of the spectroscopic-network-assisted precision spectroscopy (SNAPS) procedure.[57,58,61,62] The panels of Fig. 4 help to visualize how the new measurements connect previous floating SN components to the two principal components. The 20 newly measured lines, 11 *para* and 9 *ortho* ones, not only help to connect previously floating components to the roots of the *para* and *ortho* principal components by defining ultraprecise paths but some of them are also part of cycles, which can be utilized to confirm the accuracy of the measured lines.

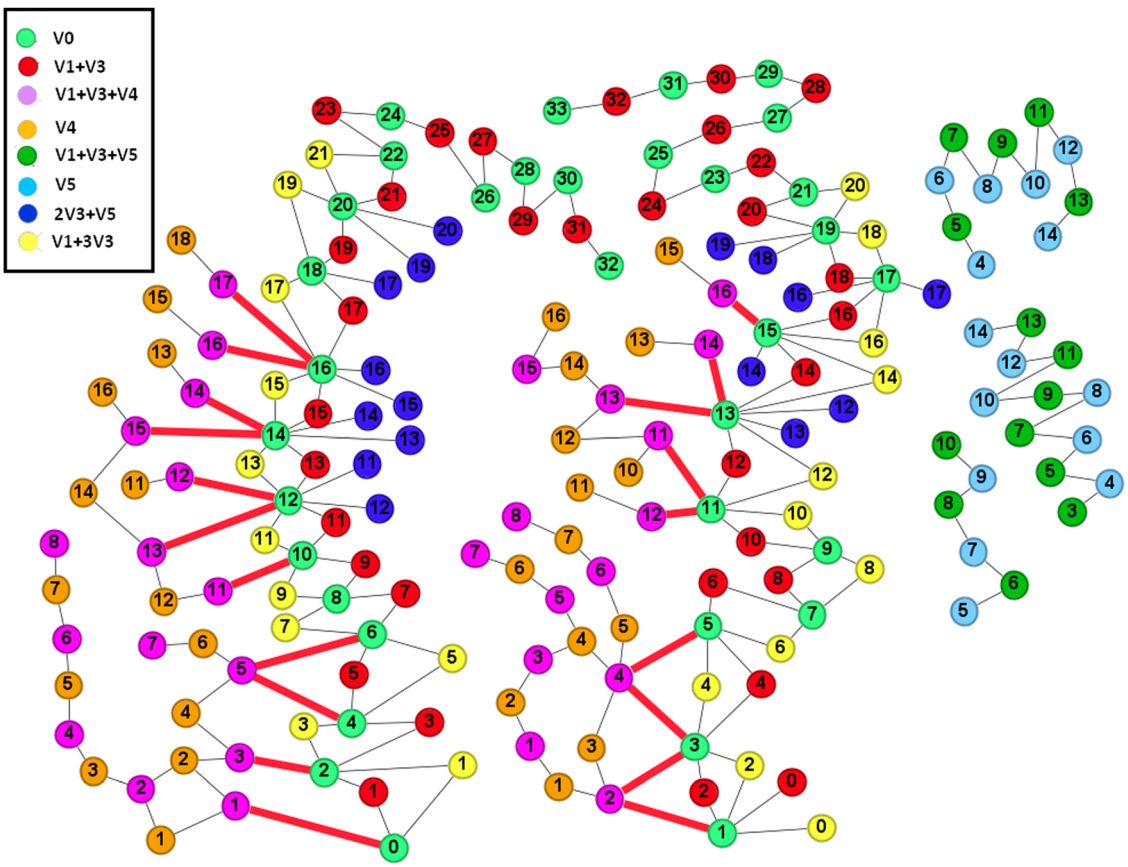

Fig. 4 Cartoon, with color-coded bands, depicting the spectroscopic network of $^{12}C_2H_2$, formed by lines measured with ultraprecision spectroscopy, assembled and investigated during this study. The red links correspond to the new measurements (see also Table 2), designed to connect previously measured floating components and orphans to the two principal components of $^{12}C_2H_2$. The *para* and *ortho* principal components are in the left and the middle of the figure, respectively, the remaining (large) floating components are in the right. For the sake of clarity, the large number of floating components with less than five transitions are not shown. Numbers within the colored dots (vertices of the spectroscopic network) correspond to the rotational quantum number J.

Table 4 Statistical data about energy levels and transitions forming the ultraprecise spectroscopic network of $^{12}C_2H_2$

Network property	Without this study	With this study
Number of transitions in the database	311	331
Number of unique transitions in the database	263	283
Number of unique transitions in the two principal components	127	195
Number of unique transitions in the two principal components under 10 000 cm^{-1}	81	149
Number of components in the database	74	63
Number of transitions in the *para* principal component	86	121
Number of transitions in the *ortho* principal component	86	119
Number of validated transitions	172	240
Number of energy levels in the database	314	314
Number of energy levels in the *para* principal component	53	82
Number of energy levels in the *ortho* principal component	52	80

As clear from Fig. 4, four *para* and nine *ortho* lines are not part of cycles; thus, their measurement accuracy cannot be confirmed this way. Nevertheless, since the majority of the newly measured lines are part of a number of cycles, the results of the uncertainty budget analysis can be accepted for all of the lines.

Table 4 summarizes the most important statistical data about the SN of precision-spectroscopy measurements assembled during this study, both with and without the lines of the present study. The ultraprecise SN of $^{12}C_2H_2$ contains transitions from the following bands: ν_4, ν_5, $\nu_1 + \nu_3$, $\nu_1 + \nu_3 + \nu_4$, $\nu_1 + \nu_3 + \nu_5$, $2\nu_3 + \nu_5$, and $\nu_1 + 3\nu_3$. The number of validated transitions is lower than the total number of transitions since we cannot validate transitions in floating components and orphans. As seen in Table 4, while originally there were 105 rovibrational energy levels within the two principal components of the SN, the 20 newly-measured lines help to connect a further 57 levels to the principal components. The different measurements nicely complement each other and thus for lower J values one can find a large number of cycles, helping to establish the true accuracy of the measurements.

4 The TenkHz line list of $^{12}C_2H_2$

The empirical rovibrational energy levels determined with the help of the MARVEL algorithm can be used to generate a rovibrational line list for $^{12}C_2H_2$. To achieve this, the usual one-photon selection rules[1] were employed to identify the transitions. The extensive set of selection rules significantly limits the number and regions of allowed transitions among the rovibrational states of $^{12}C_2H_2$. The intensities were derived from the Einstein-A coefficients of the aCeTY line list[13] of the ExoMol project. There are no transitions reported in the Exomol database[13] above 10 000 cm^{-1}; thus, the empirical energies above 12 000 cm^{-1} cannot be utilized to generate further line-list elements. We employed the value of $Q(T = 296\ K) = 412.45\,008$[63] for the total internal partition function, needed to generate the room-temperature line intensities. The complete line list is given in the ESI.†

Since there are still a relatively large number of transitions and energy levels which are not part of the two principal components (see Table 4) and since the selection rules governing the one-photon transitions are highly restrictive, one cannot expect a very large number of predicted transitions. In fact, the TenkHz line list contains 282 rovibrational transitions, the hot bands starting from ν_4 in the $\nu_1 + \nu_3$ and $\nu_1 + \nu_3 + \nu_4$ regions. 133 predicted lines, in the wavenumber range of 5898.97–7258.87 cm^{-1}, have not been measured before. Since the uncertainties of these predicted lines are about 10 kHz, these lines are perfect candidates even for metrological applications. The list of lines may also act as frequency standards over a wide frequency range, helping future high-resolution experiments.

5 Comparison with HITRAN

It is worth checking whether our new TenkHz database contains lines which are missing from the canonical spectroscopic line-by-line database HITRAN2020.[11] It is comforting to observe that 247 of the 282 predicted lines can be found in the HITRAN2020 dataset. The average deviation of these TenkHz and HITRAN2020 lines is only 6.5×10^{-4} cm^{-1}, in perfect agreement within the stated HITRAN2020 uncertainties.[11] Of course, the lines in our TenkHz database are orders of magnitude more accurate than this; thus, it is recommended to consider them during the next update of the HITRAN database.

Furthermore, the TenkHz line list contains 35 lines that are missing from the HITRAN2020 database. Since the intensity of each of these lines is larger than 4.5×10^{-30} cm molecule^{-1}, all these lines, which are in the 6524.94–6605.48 cm^{-1} region, should be considered for inclusion. Note that there are 27 lines missing from HITRAN2020[11] whose intensities, at room temperature, are between 1.5×10^{-22} and 1×10^{-26} cm molecule^{-1}.

6 Summary and conclusions

In this study, the absolute center frequencies of twenty rovibrational lines of $^{12}C_2H_2$, including 11 *para* and 9 *ortho* ones, have been measured using Lamb-dip cavity ring-down spectroscopy, assisted by a near-infrared optical frequency comb synthesizer. The spectrometer is an upgraded version of that described in ref. 32 and 48, expressly designed for extensive Lamb-dip investigations. The experimental strategy is based on spectral acquisitions as a function of the gas pressure, so that the zero-pressure center frequency could be retrieved for each of the selected transitions. The combined uncertainty, at the 2-σ confidence level, varies between 12 and 21 kHz, while the average 1-σ uncertainty amounts to about 7 kHz.

Selection of the newly measured lines, in the spectral window of 7125–7230 cm^{-1} supported by our spectrometer, is based on the theory of spectroscopic networks (SN). The few carefully selected and carefully executed new line measurements allow to attach several previously unconnected components and orphans to the two principal components of the SN of $^{12}C_2H_2$. A dataset containing 331 highly precise lines, including 283 unique ones, has been assembled, defining a network composed only of transitions measured with an accuracy better than 10 kHz (1-σ confidence level). 119 and 121 of the lines are in the *ortho* and *para* principal components, respectively, while the rest remains in floating components. Based on paths and cycles of the SN, we successfully validated all previous ultraprecise measurements, except one, 15TwCiSeMc,[27] where the uncertainties had to be increased by 50%. Then, based on the Measured Active Rotational–Vibrational Energy Levels (MARVEL) procedure, 82 and 80 ultraprecise empirical rovibrational energy levels have been determined in the *para*- and *ortho*-$^{12}C_2H_2$ principal components, involving the following five vibrational bands: ν_4, $\nu_1 + \nu_3$, $\nu_1 + \nu_3 + \nu_4{}^1$, $2\nu_3 + \nu_5$, and $\nu_1 + 3\nu_3$. The accuracy of the energy levels is similar to that of the lines.

Based on the 162 ultraprecise empirical rovibrational energies, we generated a rovibrational line list, which we call TenkHz, for $^{12}C_2H_2$, containing 282 entries in the spectral range of 5898.97–7258.87 cm^{-1}. Up to now, only 149 of these predicted transitions have been measured directly *via* precision spectroscopy. Since the accuracy of these predicted lines is better than 10 kHz, these lines are perfect candidates even for metrological applications. The list of TenkHz lines may also act as frequency standards over a wide frequency range, helping future high-resolution and precision-spectroscopy measurements. 247 of the 282 TenkHz lines can be found in the canonical spectroscopic line-by-line database HITRAN2020.[11] The average deviation of these 247 lines is only 6.5×10^{-4} cm^{-1}, in perfect agreement within the stated HITRAN2020 uncertainties. Of course, the lines in our TenkHz database are orders of magnitude more accurate than this. The intensity of 27 of the remaining 35 TenkHz lines that are missing from the HITRAN2020 database are between 1.5×10^{-22} and 1×10^{-26} cm molecule^{-1}. Thus, the present ultraprecise Lamb-dip measurements and the TenkHz line list should prove useful during the next upgrade of the HITRAN dataset on $^{12}C_2H_2$.

Despite the large number of rovibrational lines in the TenkHz line list assembled during this study, there are still a number of ways how one can improve our knowledge of the spectroscopy of acetylene at the kHz level. To this aim, future perspectives include new absolute frequency measurements of those transitions that connect the remaining floating components, such as the spectral lines of the $\nu_1 + \nu_3 + \nu_5$ band or those of the fundamental vibrational mode ν_5. In fact, ultra-accurate determinations of molecular transition frequencies can be extended to the mid-infrared spectral region by combining the technology of quantum cascade lasers with the most advanced nonlinear mixing techniques to calibrate the spectroscopic measurements by means of an optical frequency comb in the near infrared.[64,65]

Conflicts of interest

There are no conflicts to declare.

Acknowledgements

The experimental work was partially done within the project PROMETH2O (EMPIR 20IND06), which received funding from the EMPIR programme co-financed by the Participating States and from the European Unions Horizon 2020 research and innovation programme. The work performed in Budapest received support from NKFIH (grant no. K138233). This publication supports research performed within the COST Action CA21101 ''Confined molecular systems: from a new generation of materials to the stars'' (COSY), funded by the European Cooperation in Science and Technology (COST) and the MSCA Doctoral Network PHYMOL: ''Physics, accuracy and machine learning, towards the next generation of molecular potentials''.

References

1 K. L. Chubb, M. Joseph, J. Franklin, N. Choudhury, T. Furtenbacher, A. G. Császár, G. Gaspard, P. Oguoko, A. Kelly, S. N. Yurchenko, J. Tennyson and C. Sousa-Silva, *J. Quant. Spectrosc. Radiat. Transfer*, 2018, **204**, 42–55.
2 T. Furtenbacher, A. G. Császár and J. Tennyson, *J. Mol. Spectrosc.*, 2007, **245**, 115–125.
3 T. Furtenbacher and A. G. Császár, *J. Quant. Spectrosc. Radiat. Transfer*, 2012, **113**, 929–935.
4 M. Herman, A. Campargue, M. I. El Idrissi and J. Vander Auwera, *J. Phys. Chem. Ref. Data*, 2003, **32**, 921–1361.
5 M. Herman, *Mol. Phys.*, 2007, **105**, 2217–2241.
6 K. Didriche and M. Herman, *Chem. Phys. Lett.*, 2010, **496**, 1–7.
7 B. Amyay, A. Fayt, M. Herman and J. V. Auwera, *J. Phys. Chem. Ref. Data*, 2016, **45**, 023103.
8 B. J. Orr, *Int. Rev. Phys. Chem.*, 2006, **25**, 655–718.
9 D. Jacquemart, O. Lyulin and V. I. Perevalov, *J. Quant. Spectrosc. Radiat. Transfer*, 2017, **203**, 440–453.
10 O. M. Lyulin and V. I. Perevalov, *J. Quant. Spectrosc. Radiat. Transfer*, 2017, **201**, 94–103.
11 I. E. Gordon, L. S. Rothman, R. J. Hargreaves, R. Hashemi, E. V. Karlovets, F. M. Skinner, E. K. Conway, C. Hill, R. V. Kochanov, Y. Tan, P. Wcisło, A. A. Finenko, K. Nelson, P. F. Bernath, M. Birk, V. Boudon, A. Campargue, K. V. Chance, A. Coustenis, B. J. Drouin, J. Flaud, R. R. Gamache, J. T. Hodges, D. Jacquemart, E. J. Mlawer, A. V. Nikitin, V. I. Perevalov, M. Rotger, J. Tennyson, G. C. Toon, H. Tran, V. G. Tyuterev, E. M. Adkins, A. Baker, A. Barbe, E. Canè, A. G. Császár, A. Dudaryonok, O. Egorov, A. J. Fleisher, H. Fleurbaey, A. Foltynowicz, T. Furtenbacher, J. J. Harrison, J. Hartmann, V. Horneman, X. Huang, T. Karman, J. Karns, S. Kassi, I. Kleiner, V. Kofman, F. Kwabia-Tchana, N. N. Lavrentieva, T. J. Lee, D. A. Long, A. A. Lukashevskaya, O. M. Lyulin, V. Y. Makhnev, W. Matt, S. T. Massie, M. Melosso, S. N. Mikhailenko, D. Mondelain, H. S. P. Müller, O. V. Naumenko, A. Perrin, O. L. Polyansky, E. Raddaoui,

P. L. Raston, Z. D. Reed, M. Rey, C. Richard, R. Tóbiás, I. Sadiek, D. W. Schwenke, E. Starikova, K. Sung, F. Tamassia, S. A. Tashkun, J. Vander Auwera, I. A. Vasilenko, A. A. Vigasin, G. L. Villanueva, B. Vispoel, G. Wagner, A. Yachmenev and S. N. Yurchenko, *J. Quant. Spectrosc. Radiat. Transfer*, 2022, **277**, 107949.

12 T. Delahaye, R. Armante, N. A. Scott, N. Jacquinet-Husson, A. Chédin, L. Crépeau, C. Crevoisier, V. Douet, A. Perrin, A. Barbe, V. Boudon, A. Campargue, L. Coudert, V. Ebert, J.-M. Flaud, R. R. Gamache, D. Jacquemart, A. Jolly, F. K. Tchana, A. Kyuberis, G. Li, O. M. Lyulin, L. Manceron, S. Mikhailenko, N. Moazzen-Ahmadi, H. S. P. Müller, O. V. Naumenko, A. Nikitin, V. I. Perevalov, C. Richard, E. Starikova, S. A. Tashkun, V. G. Tyuterev, J. V. Auwera, B. Vispoel, A. Yachmenev and S. Yurchenko, *J. Mol. Spectrosc.*, 2021, **380**, 111510.

13 K. L. Chubb, J. Tennyson and S. N. Yurchenko, *Mon. Not. R. Astron. Soc.*, 2020, **493**, 1531–1545.

14 J. Ye, L.-S. Ma and J. L. Hall, *Opt. Lett.*, 1996, **21**, 1000–1002.

15 R. Aiello, V. Di Sarno, M. G. Delli Santi, M. De Rosa, I. Ricciardi, G. Giusfredi, P. De Natale, L. Santamaria and P. Maddaloni, *Photon. Res.*, 2022, **10**, 1803–1809.

16 A. Albert Schliesser, N. Picqué and T. W. Haensch, *Nat. Photonics*, 2012, **6**, 440.

17 A. Gambetta, E. Vicentini, N. Coluccelli, Y. Wang, T. T. Fernandez, P. Maddaloni, P. De Natale, A. Castrillo, L. Gianfrani, P. Laporta and G. Galzerano, *APL Photonics*, 2018, **3**, 046103.

18 W. J. Lafferty, R. D. Suenram and D. R. Johnson, *J. Mol. Spectrosc.*, 1977, **64**, 147–156.

19 K. Nakagawa, M. de Labachelerie, Y. Awaji and M. Kourogi, *J. Opt. Soc. Am. B*, 1996, **13**, 2708.

20 C. S. Edwards, H. S. Margolis, G. P. Barwood, S. N. Lea, P. Gill, G. Huang and W. R. C. Rowley, *Opt. Lett.*, 2004, **29**, 566.

21 C. S. Edwards, G. P. Barwood, H. S. Margolis, P. Gill and W. R. C. Rowley, *J. Mol. Spectrosc.*, 2005, **234**, 143–148.

22 A. A. Madej, A. J. Alcock, A. Czajkowski, J. E. Bernard and S. Chepurov, *J. Opt. Soc. Am. B*, 2006, **23**, 2200–2208.

23 A. A. Madej, J. E. Bernard, A. J. Alcock, A. Czajkowski and S. Chepurov, *J. Opt. Soc. Am. B*, 2006, **23**, 741.

24 K. Knabe, S. Wu, J. Lim, K. A. Tillman, P. S. Light, F. Couny, N. Wheeler, R. Thapa, A. M. Jones, J. W. Nicholson, B. R. Washburn, F. Benabid and K. L. Corwin, *Opt. Expr.*, 2009, **17**, 16017–16026.

25 S. Yu, B. J. Drouin and J. C. Pearson, *Astrophys. J.*, 2009, **705**, 786–790.

26 C. Wang, N. V. Wheeler, C. Fourcade-Dutin, M. Grogan, T. D. Bradley, B. R. Washburn, F. Benabid and K. L. Corwin, *Appl. Opt.*, 2013, **52**, 5430–5439.

27 S. Twagirayezu, M. J. Cich, T. J. Sears, C. P. McRaven and G. E. Hall, *J. Mol. Spectrosc.*, 2015, **316**, 64–71.

28 E. Fasci, T. A. Odintsova, A. Castrillo, M. D. D. Vizia, A. Merlone, F. Bertiglia, L. Moretti and L. Gianfrani, *Phys. Rev. A*, 2016, **93**, 042513.

29 D. Gatti, R. Gotti, A. Gambetta, M. Belmonte, G. Galzerano, P. Laporta and M. Marangoni, *Sci. Rep.*, 2016, **6**, 27183.

30 L.-G. Tao, T.-P. Hua, Y. R. Sun, J. Wang, A.-W. Liu and S.-M. Hu, *J. Quant. Spectrosc. Radiat. Transfer*, 2018, **210**, 111–115.

31 S. Twagirayezu, G. E. Hall and T. J. Sears, *J. Chem. Phys.*, 2018, **149**, 154308.

32 E. Fasci, S. Gravina, G. Porzio, A. Castrillo and L. Gianfrani, *New J. Phys.*, 2021, **23**, 123023.

33 R. Aiello, V. Di Sarno, M. G. Delli Santi, M. De Rosa, I. Ricciardi, P. De Natale, L. Santamaria, G. Giusfredi and P. Maddaloni, *Nat. Commun.*, 2022, **13**, 7016.

34 J. Plíva, *J. Mol. Spectrosc.*, 1972, **44**, 165–182.

35 A.-M. Tolonen and S. Alanko, *Mol. Phys.*, 1992, **75**, 1155–1165.

36 R. Hashemi, C. Povey, M. Derksen, H. Naseri, J. Garber and A. Predoi-Cross, *J. Chem. Phys.*, 2014, **141**, 214201.

37 A. Castrillo, E. Fasci, H. Dinesan, S. Gravina, L. Moretti and L. Gianfrani, *Phys. Rev. Appl.*, 2019, **11**, 064060.

38 P. B. Rimmer, M. Ferus, I. P. Waldmann, A. Knížek, D. Kalvaitis, O. Ivanek, P. Kubelík, S. N. Yurchenko, T. Burian, J. Dostál, L. Juha, R. Dudžák, M. Krůs, J. Tennyson, S. Civiš, A. T. Archibald and A. Granville-Willett, *Astrophys. J.*, 2019, **888**, 21.

39 D. Gasman, M. Min and K. L. Chubb, *A&A*, 2022, **659**, A114.

40 Z. D. Reed, D. A. Long, H. Fleurbaey and J. T. Hodges, *Optica*, 2020, **7**, 1209–1220.

41 E. Fasci, A. Castrillo, H. Dinesan, S. Gravina, L. Moretti and L. Gianfrani, *Phys. Rev. A*, 2018, **98**, 022516.

42 L.-G. Tao, A.-W. Liu, K. Pachucki, J. Komasa, Y. R. Sun, J. Wang and S.-M. Hu, *Phys. Rev. Lett.*, 2018, **120**, 153001.

43 A. G. Császár and T. Furtenbacher, *J. Mol. Spectrosc.*, 2011, **266**, 99–103.

44 T. Furtenbacher, P. Árendás, G. Mellau and A. G. Császár, *Sci. Rep.*, 2014, **4**, 4654.

45 A. G. Császár, T. Furtenbacher and P. Árendás, *J. Phys. Chem. A*, 2016, **120**, 8949–8969.

46 R. Tóbiás, T. Furtenbacher and A. G. Császár, *J. Quant. Spectrosc. Radiat. Transfer*, 2017, **203**, 557–564.

47 H. Dinesan, E. Fasci, A. D'Addio, A. Castrillo and L. Gianfrani, *Opt. Expr.*, 2015, **23**, 1757–1766.

48 E. Fasci, H. Dinesan, L. Moretti, A. Merlone, A. Castrillo and L. Gianfrani, *Metrologia*, 2018, **55**, 662–669.

49 G. Giusfredi, S. Bartalini, S. Borri, P. Cancio, I. Galli, D. Mazzotti and P. De Natale, *Phys. Rev. Lett.*, 2010, **104**, 110801.

50 B. I. des Poids et Mesures (BIPM), *CCQM Guidance note: Estimation of a consensus KCRV and associated Degrees of Equivalence*, 2013, **https://www.bipm.org/documents/20126/28430045/working-document-ID-5794/49d366bc-295f-18ca-c4d3-d68aa54077b5**.

51 J. L. Hall, C. J. Bordé and K. Uehara, *Phys. Rev. Lett.*, 1976, **37**, 1339–1342.

52 V. D. Sarno, R. Aiello, M. D. Rosa, I. Ricciardi, S. Mosca, G. Notariale, P. D. Natale, L. Santamaria and P. Maddaloni, *Optica*, 2019, **6**, 436–441.

53 J. Chen, T.-P. Hua, L.-G. Tao, Y. Sun, A.-W. Liu and S.-M. Hu, *J. Quant. Spectrosc. Radiat. Transfer*, 2018, **205**, 91–95.

54 F. M. J. Cozijn, P. Dupré, E. J. Salumbides, K. S. E. Eikema and W. Ubachs, *Phys. Rev. Lett.*, 2018, **120**, 153002.

55 W. Ma, A. Foltynowicz and O. Axner, *J. Opt. Soc. Am. B*, 2008, **25**, 1144–1155.

56 L.-S. Ma, J. Ye, P. Dubé and J. L. Hall, *J. Opt. Soc. Am. B*, 1999, **16**, 2255–2268.

57 R. Tóbiás, T. Furtenbacher, I. Simkó, A. G. Császár, M. L. Diouf, F. M. J. Cozijn, J. M. A. Staa, E. J. Salumbides and W. Ubachs, *Nat. Commun.*, 2020, **11**, 1708.
58 M. L. Diouf, R. Tóbiás, I. Simkó, F. M. J. Cozijn, E. J. Salumbides, W. Ubachs and A. G. Császár, *J. Phys. Chem. Ref. Data*, 2021, **50**, 023106.
59 M. E. J. Newman, *Networks*, Oxford University Press, Oxford, 2010.
60 BIPM report, **https://www.bipm.org/en/publications/mises-en-pratique/standard-frequencies-metre**.
61 M. L. Diouf, R. Tóbiás, T. S. van der Schaaf, F. M. J. Cozijn, E. J. Salumbides, A. G. Császár and W. Ubachs, *Mol. Phys.*, 2022, **120**, 1.
62 M. L. Diouf, R. Tóbiás, F. M. J. Cozijn, E. J. Salumbides, C. Fábri, C. Puzzarini, A. G. Császár and W. Ubachs, *Opt. Expr.*, 2022, **30**, 46040.
63 R. R. Gamache, B. Vispoel, M. Rey, A. Nikitin, V. Tyuterev, O. Egorov, I. E. Gordon and V. Boudon, *J. Quant. Spectrosc. Radiat. Transfer*, 2021, **271**, 107713.
64 A. Gambetta, D. Gatti, A. Castrillo, G. Galzerano, P. Laporta, L. Gianfrani and M. Marangoni, *Appl. Phys. Lett.*, 2011, **99**, 251107.
65 A. Gambetta, N. Coluccelli, M. Cassinerio, T. T. Fernandez, D. Gatti, A. Castrillo, A. Ceausu-Velcescu, E. Fasci, L. Gianfrani, L. Santamaria, V. D. P. Maddaloni, P. De Nataleand, P. Laporta and G. Galzerano, *J. Chem. Phys.*, 2015, **143**, 234202.